

## Quantitative moment study and coupling of 4*f* rare earth and 3*d* metal by transmitted electrons

X. Fu,<sup>1</sup> B. Warot-Fonrose,<sup>1</sup> R. Arras,<sup>1</sup> K. Dumesnil,<sup>2</sup> and V. Serin<sup>1</sup>

<sup>1</sup>*Université Toulouse, CEMES-CNRS UPR 8011, F-31055 Toulouse, France*

<sup>2</sup>*Institut Jean Lamour (UMR CNRS 7198), Université H. Poincaré-Nancy I,*

*Boîte Postale 239, 54506 Vandoeuvre-les-Nancy Cedex, France*

(Received 6 September 2016; published 27 October 2016)

We report a simultaneous investigation of 3*d* and 4*f* magnetic moments by exploring the Fe- $L_{2,3}$  and Dy- $M_{4,5}$  electron energy-loss edges of a DyFe<sub>2</sub>/YFe<sub>2</sub> superlattice using the energy-loss magnetic chiral dichroism (EMCD) technique. Specific EMCD sum rules for  $M_{4,5}$  edges were established and carefully applied to the dichroic signal at Dy- $M_{4,5}$  edges, giving an orbital to the effective spin moment ratio of  $5.1 \pm 1.8$ . With dynamic diffraction effects considered, the opposite signs of Fe- $L_3$  and Dy- $M_5$  dichroic peaks unambiguously indicate the antiparallel alignment of net Fe 3*d* and Dy 4*f* moments. The EMCD technique is shown to be an effective tool to locally characterize the 4*f* moment of rare earth elements and study 3*d*-4*f* moment coupling.

DOI: [10.1103/PhysRevB.94.140416](https://doi.org/10.1103/PhysRevB.94.140416)

The alloys, compounds, or other systems consisting of rare earth (RE) and 3*d* transition metals (TMs) are of high interest for their current and potential applications in permanent magnets and magnetic recording media [1,2]. For such materials with multiple magnetic elements, measurement techniques with elemental resolution are required for studying the magnetic coupling and revealing the origin of some magnetic properties [3,4]. In recent decades, element-specific x-ray magnetic circular dichroism (XMCD) has been commonly applied to these materials to separately probe TM 3*d* and RE 4*f* moments [3–6]. As a counterpart of synchrotron-based XMCD, energy-loss magnetic chiral dichroism (EMCD) based on transmission electron microscopy (TEM) is also a technique to measure the element-specific orbital and spin moments with applying sum rules [7–9]. Compared to XMCD, EMCD may uniquely achieve magnetic moment information with high spatial resolution, down to 1 nm or even less in the ultimate case of tailored beams [10,11] and is capable of simultaneously obtaining morphology, local atomic structure, and chemical components in a TEM [12]. EMCD has thus great potential in the study of complex nanostructures with multiple magnetic elements and nonhomogeneous magnetic configurations or one element presenting different moments. With these promising prospects, EMCD has been constantly improved; however more effort is still required to study TM-RE systems with this technique. First, although EMCD experiments have been extensively performed on  $L_{2,3}$  ( $2p_{1,2,3/2} \rightarrow 3d_{3,2,5/2}$ ) edges of 3*d* TM [8,9,11,13–15] in recent years,  $M_{4,5}$  ( $3d_{3,2,5/2} \rightarrow 4f_{5,2,7/2}$ ) edges of 4*f* RE rarely have been investigated. Moreover, differing from XMCD, the EMCD signal is influenced by dynamical electron diffraction effects [8,9,16]. Thus special attention should be paid to the acquisition and interpretation of EMCD signals from TM 3*d* and RE 4*f* moments when investigating the coupling behavior in the system.

In this Rapid Communication, we apply EMCD to a single-crystalline DyFe<sub>2</sub>/YFe<sub>2</sub> superlattice, which is a model TM-RE system with nonhomogeneous magnetic configurations, such as an exchange spring [6] demonstrated under a magnetic field, owing to exchange couplings. 4*f* and 3*d* moments are simultaneously probed by studying Dy- $M_{4,5}$

and Fe- $L_{2,3}$  electron energy-loss (EEL) edges, respectively. Specific EMCD sum rules for  $M_{4,5}$  edges are established and applied to Dy- $M_{4,5}$  edges. The EMCD signals of Dy and Fe are compared to reveal the magnetic configuration. This study constitutes a first important step in the use of EMCD for investigating nanosystems based on RE-TM components, and the next phase will be to combine it with the high spatial resolution that can be uniquely achieved in a TEM.

The single-crystalline DyFe<sub>2</sub>/YFe<sub>2</sub> superlattices were grown using solid-source molecular-beam epitaxy on (1120) orientated sapphire substrates, covered by a 50-nm (110) niobium chemical buffer layer and a 2-nm iron seed layer subsequently [6]. A TEM cross-sectional specimen was prepared to investigate the crystallographic structure and local magnetic properties. TEM studies were performed on a Tecnai F20 microscope operating at 200 kV, fitted with an objective lens aberration corrector and imaging filter (Gatan Tridiem). The sample was submitted to a 2-T magnetic field due to the objective lens. The EMCD experimental configuration is demonstrated in Fig. 1. A large-angle convergent diffraction configuration is fulfilled to obtain a diffraction pattern corresponding to a three-beam condition on the image plane, and the energy spectrum imaging (ESI) technique is applied to record data cubes [13]. The data cubes contain a series of energy-filtered diffraction patterns with an energy window of 1 eV running over the investigated Fe- $L_{2,3}$  and Dy- $M_{4,5}$  edges. Two virtual apertures are accurately positioned in positions 1 and 2 on each postcorrected data cube to obtain two reconstructed EELS spectra [13]. At the two positions, different combinations of two electron scattering vectors  $q$  and  $q'$  give rise to left- and right-handed polarized virtual photons, which are analogs to the circularly polarized x ray in XMCD [11,13]. The magnetic moment information is then extracted from the difference spectrum called the EMCD spectrum.

To realize the simultaneous investigation of Fe and Dy sites with EMCD, suitable diffraction spots corresponding to suitable experimental diffraction conditions have to be carefully chosen. The crystal structure of the superlattice must be first studied. TEM imaging and diffraction of the specimen are demonstrated in Fig. 2. We see from Figs. 2(a) and 2(d) that two different types of layers, exhibiting intensity contrasts,

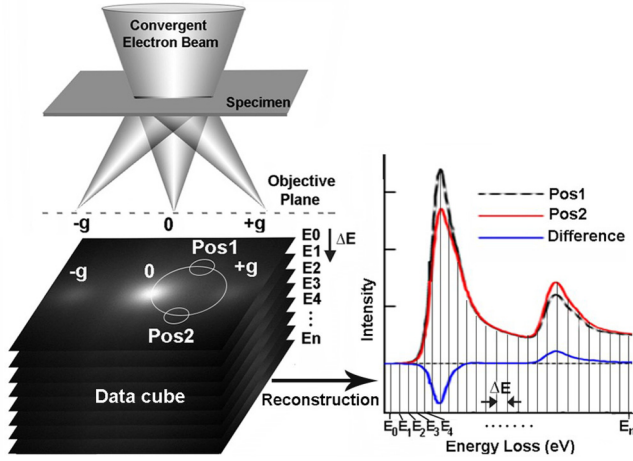


FIG. 1. Schematic of the EMCD experimental configuration using the ESI technique.

$$F_{hkl(\text{Dy})} = \sum_i f_{i(\text{Dy})} e^{2\pi i(h+k+l)} = f_{hkl(\text{Dy})} [1 + e^{(\pi i/2)(h+k+l)}] [1 + e^{\pi i(h+k)} + e^{\pi i(h+l)} + e^{\pi i(k+l)}], \quad (1)$$

$$F_{hkl(\text{Fe})} = \sum_i f_{i(\text{Fe})} e^{2\pi i(h+k+l)} = f_{hkl(\text{Fe})} e^{(\pi i/4)(h+k+l)} [e^{\pi i(h+k+l)} + e^{\pi ih} + e^{\pi ik} + e^{\pi il}] \times [1 + e^{(\pi i/2)(h+k)} + e^{(\pi i/2)(h+l)} + e^{(\pi i/2)(k+l)}], \quad (2)$$

where  $h, k, l$  are all integers and  $f_{hkl(\text{Dy})}$  and  $f_{hkl(\text{Fe})}$  are the atomic scattering amplitudes for Dy and Fe atoms, respectively.

The calculated structure factors for several diffraction spots are listed in Table I. Given that  $(11\bar{3})$  and  $(11\bar{1})$  spots have nonzero values for both  $F_{hkl(\text{Dy})}$  and  $F_{hkl(\text{Fe})}$ , they contain information from both Dy and Fe sites and are of interest for our EMCD experiment. Moreover, the  $(11\bar{3})$  spot has a much higher intensity than the  $(11\bar{1})$  spot as seen in Fig. 2(d) and is thus preferred.

In the  $(11\bar{3})$  three-beam condition, more than 20 data cubes were recorded to achieve enough statistics. Typical EELS and EMCD spectra measured at room temperature are presented in Fig. 3. Dichroism for both Fe and Dy elements is observed. The dichroism for the RE element, similar to TM, basically originates from the  $M_J$  states unequal occupation determined by the competition between Zeeman splitting energy and thermal fluctuation [3,18]. Furthermore, despite the weak but clearly visible signal at the Dy- $M_5$  and Dy- $M_4$  edges, it is of interest to note that the dichroic signal has a positive sign at the Fe- $L_3$  peak and a negative one at Fe- $L_2$ , whereas it has a negative sign at both Dy- $M_5$  and Dy- $M_4$  peaks. For XMCD, such opposite signs as those observed at the Fe- $L_3$  and Dy- $M_5$  edges generally indicate the antiparallel alignment of the two magnetic moments [3,4,19,20]. However for EMCD, it may not be necessarily true due to dynamic diffraction effects. The physical meaning of the signals here needs to be interpreted by EMCD sum rules.

The EMCD sum rules for the  $L_{2,3}$  edges of 3d TM ions or atoms, such as Fe have been established [8] and already

appear alternatively to form a superlattice with a bilayer repeat distance of about 18.8 nm. Elemental maps of Dy and Fe with energy-dispersive x-ray spectroscopy (EDX) in Figs. 2(b) and 2(c) clearly identify the DyFe<sub>2</sub> layers. Seen in the high-resolution TEM image in Fig. 2(d), the interfaces between layers, observed along the  $[1\bar{1}0]$  direction, appear rather flat and clean as DyFe<sub>2</sub> and YFe<sub>2</sub> compounds have the same C15 Laves phase structure and very close lattice constants at room temperature [17]. A DyFe<sub>2</sub> (YFe<sub>2</sub>) unit cell, space-group  $Fd\bar{3}m$ , contains eight Dy(Y) atoms in a face-centered-cubic diamond lattice and 16 Fe atoms in tetrahedrons [17] as shown in the inset in Fig. 2(d). Accordingly the diffraction patterns of DyFe<sub>2</sub> and YFe<sub>2</sub> are superimposed, and the calculation hereafter will be made only for DyFe<sub>2</sub>. A diffraction pattern, acquired through several bilayers, is displayed in the inset of Fig. 2(d).

The structure factors  $F_{hkl}$  of Dy and Fe atoms, providing in particular the information on the contributions to each specific diffraction spot, have then to be calculated. The expressions are given in Eqs. (1) and (2),

applied. The sum rule for the spin-to-orbital moment ratio [8] is given in Eq. (3),

$$\frac{\int_{L_3} (\sigma_2 - \sigma_1) dE - 2 \int_{L_2} (\sigma_2 - \sigma_1) dE}{\int_{L_3+L_2} (\sigma_2 - \sigma_1) dE} = \frac{4\langle S_z \rangle + 14\langle T_z \rangle}{3\langle L_z \rangle}, \quad (3)$$

where  $\sigma_2 - \sigma_1$  is the spectra difference,  $\langle L_z \rangle, \langle S_z \rangle, \langle T_z \rangle$  are the ground-state values of the orbital momentum, the spin momentum, and the magnetic dipole operators, respectively. Equation (3) results from the combination of the  $\langle L_z \rangle$  orbital sum rule and the  $\langle S_z \rangle$  spin sum rule in which there is a  $K$  factor containing all the information related to dynamic diffraction effects. This factor is canceled in Eq. (3).

The EMCD sum rules for  $L_{2,3}$  edges can however not be applied to Dy- $M_{4,5}$  edges as they characterize different electron transition processes. Specific rules for  $M_{4,5}$  edges are required. First, it has been confirmed that the EMCD sum rules for  $M_{4,5}$  edges can also be extended from the XMCD ones [21]. In general with XMCD sum rules [3,22,23], there are three variables:  $l$  and  $L$  denoting the orbital quantum number of the core and valence shells involved in the  $l \rightarrow L$  dipole electron transition and  $N_h$  denoting the number of holes in the valence shell. The  $L_{2,3}$  edges correspond to the electron transition from  $l = 1$  to  $L = 2$  whereas the  $M_{4,5}$  edges correspond to the transition from  $l = 2$  to  $L = 3$ . Then starting from the general XMCD sum rules and using the same procedure as in Refs. [8,24], we derived the  $\langle S_z \rangle, \langle L_z \rangle$ , and  $\langle S_z \rangle / \langle L_z \rangle$  sum rules for the  $M_{4,5}$  edges. The Supplemental Material [25] details the useful derivation steps, and the results are presented in Eqs. (4)–(6). It is equivalent to the development of Ref. [21].

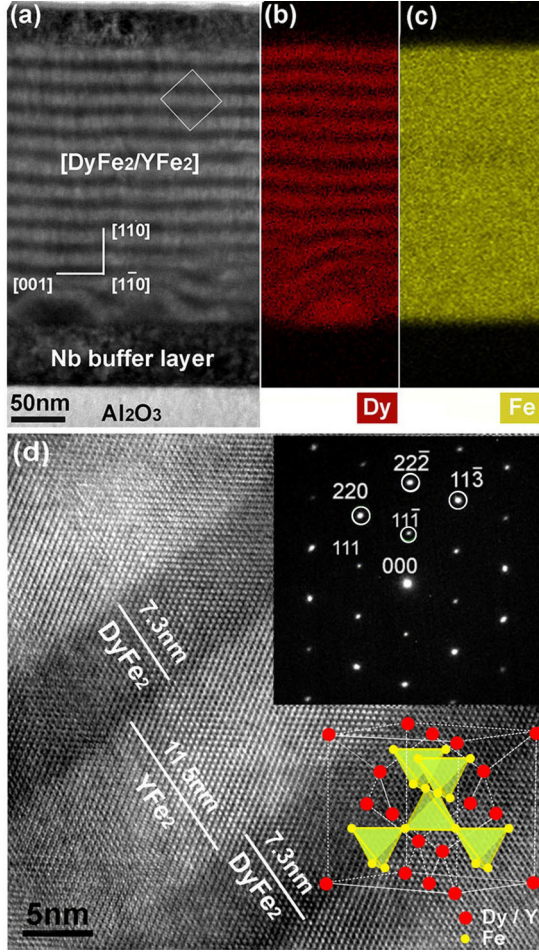


FIG. 2. (a) Low-magnification TEM image of the DyFe<sub>2</sub>/YFe<sub>2</sub> superlattice observed along the [110] zone axis, (b) and (c) EDX elemental maps of Dy and Fe, and (d) high-resolution TEM image from the area marked by a square in (a), a diffraction pattern acquired along the [110] zone axis, and a sketch of the unit cell of DyFe<sub>2</sub>(YFe<sub>2</sub>) are given in the inset.

We notice that  $K$  appears in Eqs. (4) and (5) as in the  $\langle S_z \rangle$  and  $\langle L_z \rangle$  sum rules for the  $L_{2,3}$  edges,

$$\frac{2 \int_{M_5} (\sigma_2 - \sigma_1) dE - 3 \int_{M_4} (\sigma_2 - \sigma_1) dE}{\int_{M_5+M_4} (\sigma_2 + \sigma_1) dE} = K \left( \frac{4 \langle S_z \rangle}{3 N_h} + 4 \frac{\langle T_z \rangle}{N_h} \right), \quad (4)$$

$$\frac{\int_{M_5+M_4} (\sigma_2 - \sigma_1) dE}{\int_{M_5+M_4} (\sigma_2 + \sigma_1) dE} = K \frac{1 \langle L_z \rangle}{3 N_h}, \quad (5)$$

$$\frac{2 \int_{M_5} (\sigma_2 - \sigma_1) dE - 3 \int_{M_4} (\sigma_2 - \sigma_1) dE}{\int_{M_5+M_4} (\sigma_2 - \sigma_1) dE} = \frac{4 \langle S_z \rangle + 12 \langle T_z \rangle}{\langle L_z \rangle}. \quad (6)$$

TABLE I. Structure factors of Dy and Fe in the DyFe<sub>2</sub> lattice for several diffraction spots.

$F_{hkl}$	(220)	(22 $\bar{2}$ )	(11 $\bar{3}$ )	(11 $\bar{1}$ )
Dy	$8f_{220(\text{Dy})}$	0	$4(1-i)f_{11\bar{3}(\text{Dy})}$	$4(1+i)f_{11\bar{1}(\text{Dy})}$
Fe	0	$16if_{22\bar{2}(\text{Fe})}$	$4\sqrt{2}(1-i)f_{11\bar{3}(\text{Fe})}$	$-4\sqrt{2}(1+i)f_{11\bar{1}(\text{Fe})}$

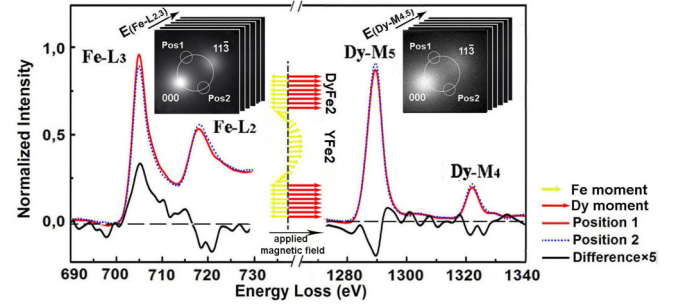


FIG. 3. EELS signals, EMCD signals, and corresponding data cubes of Fe- $L_{2,3}$  edges and Dy- $M_{4,5}$  edges under a 2-T magnetic field applied parallel to the beam axis at room temperature. The sketch in the middle shows the possible configuration of Fe and Dy moments.

With sum rules for the  $L_{2,3}$  and  $M_{4,5}$  edges, we first discuss the possible antiparallel alignment between Dy and Fe moments. Following the XMCD demonstration in Refs. [3,4,19,20] and according to Eq. (4) for Dy and its equivalent for Fe [8], a clear conclusion on the Dy and Fe moment relative orientations can be addressed if the signs of  $K$  for both edges are determined.  $K$  not only is dependent on the sample properties including the crystal structure, locations of ionized atoms in the lattice, and the local thickness, but also is influenced by experimental conditions, namely, the sample orientation, the excitation error of the incident beam, the detector position, and the aperture size [8]. In our experiment, the Fe- $L_{2,3}$  and Dy- $M_{4,5}$  edges were obtained in the same experimental conditions: the same area of around 50-nm thick with exactly the same crystal orientation. Detectors with the same aperture size were also precisely positioned in the post-treatment process. That happens to be one of the most outstanding advantages of the ESI recording method. As to the sample structural properties, the locations of ionized Fe and Dy atoms differ. Setting all our specific experimental conditions and sample structural properties mentioned above, we calculated the dichroic signals for Fe and Dy using the “BW” program developed by Löffler and Schattschneider [26]. The thickness-dependent dichroism [27] calculated by this program additionally is presented in the Supplemental Material [25]. From the calculation, we confirm that the dichroic signals for Fe and Dy have the same sign in the default condition of parallel alignment of Fe and Dy moments. Therefore, the opposite signs in Fig. 3 are not ascribed to  $K$  but unambiguously indicate an antiparallel alignment of net Fe 3d and Dy 4f moments.

This conclusion however does not necessarily reveal an antiparallel orientation between all Fe 3d and Dy 4f moments. The investigated area actually covers about three bilayers, so the Fe signal comes from both DyFe<sub>2</sub> and YFe<sub>2</sub>. It is known that under a zero magnetic field, Fe moments in DyFe<sub>2</sub> layers are antiparallel to Dy moments and parallel to Fe moments in YFe<sub>2</sub> layers [28] for minimizing the exchange energy. With a suitable applied field, the DyFe<sub>2</sub>/YFe<sub>2</sub> superlattice may form an exchange spring [6] where only Fe moments in the core of YFe<sub>2</sub> layers twist towards the applied field. In our experiment, a 2-T magnetic field is applied nearly along the [110] zone axis. In this case, concerning the room temperature and the DyFe<sub>2</sub>/YFe<sub>2</sub> relative thicknesses,

previous superconducting quantum interference device and XMCD measurements performed for similar samples [6,28] have revealed a homogeneous ferromagnetic order of dominant Dy moments pointing towards the field and an inhomogeneous twisted order of Fe moments as shown in the inset of Fig. 3.

The sum rules can then be applied to the dichroic signals at the Fe- $L_{2,3}$  and Dy- $M_{4,5}$  edges. Three important points have first to be underlined here before giving quantitative values. The first point is the validity and accuracy of the sum rules. The XMCD  $\langle S_z \rangle$  sum rule strictly requires that the core spin-orbit splitting is sufficiently large compared with other interactions including mainly the core-valence exchange interaction [29,30]. We assume it also true for EMCD as the EMCD sum rules are derived from XMCD. To be more specific, the Fe- $L_3$  and Fe- $L_2$  edges have to correspond to pure  $2p_{3/2}$  and  $2p_{1/2}$ , respectively, and similarly  $M_5$  and  $M_4$  edges correspond to pure  $3d_{5/2}$  and  $3d_{3/2}$  states [30]. In the real situation, the mixing between two  $p$  states exists due to the  $2p$ - $3d$  exchange interaction for Fe, illustrating an overlapping region in  $L_3$  and  $L_2$  edges. The spin moment of Fe calculated with the  $\langle S_z \rangle$  sum rule is thus precise within 5%–10% [31]. Fortunately the  $3d$ - $4f$  exchange interaction is negligible for heavy  $4f$  moments, such as Dy, which has a sufficient energy gap between  $M_5$  and  $M_4$  edges owing to the strong spin-orbit coupling [30]. We thus consider sum rules for the Dy- $M_{4,5}$  edges as valid and accurate. Second, an important assumption was made in the derivation of the EMCD sum rules [8,21]: All magnetic moments are aligned along the  $z$  axis, which is parallel to the TEM beam axis, otherwise the obtained moment is the component projected along the  $z$  axis. As previously discussed, Dy moments are aligned along  $z$ , but Fe moments can form a spring in our experimental condition. The Fe moment obtained from the dichroic signal is thus a  $z$ -component moment. The third point is that the strong spin-orbit coupling in a  $4f$  element makes  $\langle T_z \rangle$  in Eqs. (4) and (6) non-negligible. The  $\langle L_z \rangle / \langle S_z \rangle$  value of Dy can therefore hardly be obtained by directly applying Eq. (6) to the dichroic signal. We instead estimate the ratio of  $\langle L_z \rangle$  to the effective spin moment defined by  $\langle S_{z \text{ eff}} \rangle = \langle S_z \rangle + 3\langle T_z \rangle$  for Dy. For  $3d$  TM atoms or ions,  $\langle T_z \rangle$  is negligible compared to  $\langle S_z \rangle$  [23], so we consider the effective spin moment for Fe  $\langle S_{z \text{ eff}} \rangle = \langle S_z \rangle + 7/2\langle T_z \rangle$  [Eq. (3)] nearly equivalent to  $\langle S_z \rangle$ .

The measured  $\langle L_z \rangle / \langle S_z \rangle$  value of Fe is  $0.20 \pm 0.05$ , and the  $\langle L_z \rangle / \langle S_{z \text{ eff}} \rangle$  of Dy is  $5.1 \pm 1.8$ . The error is estimated by the standard deviation on the results of selected data cubes. It mainly originates from a relatively low signal-to-noise ratio. Slight deviations from the perfect three-beam condition, postnormalization, aperture size, and plural scattering also play roles, and experiments have been performed in previously optimized conditions [15,32]. The experimental value of Dy is

larger than the theoretical value of 1.40, calculated via density functional theory and the local spin-density approximation using the full-potential linearized augmented plane-wave-code WIEN2K [33]. For comparison, a  $\langle L_z \rangle / \langle S_{z \text{ eff}} \rangle$  value of 1.82 has been numerically calculated in Ref. [30] for  $\text{Dy}^{3+}$ . The discrepancy between our experimental and theoretical values may mainly result from the oversimplification of theoretical calculations which are based on the atomic ground state at  $T = 0\text{K}$ . For Dy, the lower Zeeman level  $M_J = -15/2$  is mainly occupied with negligible influence of thermal energy at low temperatures close to 0 K, whereas at room temperature, other higher-lying states are also occupied, making the dichroism inevitably vary [3]. Additionally in recent XMCD experiments for  $\text{DyCo}_3$ , a  $\langle L_z \rangle / \langle S_{z \text{ eff}} \rangle$  value of  $4.36 \pm 0.40$  for the Dy ion at 300 K was reported [3]. Given the rather high dispersion of the published results, we can consider our EMCD value as on the same order of magnitude with the XMCD value reported for the Dy ion in  $\text{DyCo}_3$ . For Fe, a careful comparison between the experimental and the theoretical values cannot easily be made since the dichroic signal of Fe results from an inhomogeneous configuration of Fe moments.

In conclusion, we applied the EMCD technique to the single-crystalline  $\text{DyFe}_2/\text{YFe}_2$  superlattice, simultaneously probing Fe and Dy sites by investigating Fe- $L_{2,3}$  edges and particularly Dy- $M_{4,5}$  edges in a TEM. Referring to the calculated structure factors, the  $(11\bar{3})$  three-beam condition was specially set for the EMCD signal acquisition. Dichroic signals of both elements were observed, and opposite signs at Fe- $L_3$  and Dy- $M_5$  peaks were noticed. Specific EMCD sum rules for the  $M_{4,5}$  edges, different from those for the  $L_{2,3}$  edges, were obtained and discussed in detail. The orbital to effective spin moment ratios of Dy and Fe were then determined by applying respective sum rules. Additionally, the opposite signs of Fe- $L_3$  and Dy- $M_5$  peaks have been proved to indicate antiparallel alignment between net Fe and Dy moments with dynamic diffraction effects considered. The EMCD technique is now verified to be an effective tool to probe  $4f$  moments and investigate the  $3d$ - $4f$  coupling in a RE-TM system. The coming progress to achieve the simultaneous high spatial resolution will make EMCD a more efficient tool for the local investigation of magnetic moments and magnetic coupling, a complementary technique to XMCD experiments.

This work was supported by the French National Project EMMA (Project No. ANR12 BS10 013 01) and by the European Union under the Seventh Framework Program under a contract for an Integrated Infrastructure Initiative Reference No. 312483-ESTEEM2. The authors of this Rapid Communication were granted access to the HPC resources of CALMIP under the allocations P1509. The authors would like to thank S. Löffler for providing the BW program and making valuable discussions.

- [1] W. E. Wallace, *Prog. Solid State Chem.* **16**, 127 (1985).  
 [2] C. D. Stanciu, F. Hansteen, A. V. Kimel, A. Kirilyuk, A. Tsukamoto, A. Itoh, and T. Rasing, *Phys. Rev. Lett.* **99**, 047601 (2007).

- [3] K. Chen, D. Lott, F. Radu, F. Choueikani, E. Otero, and P. Ohresser, *Phys. Rev. B* **91**, 024409 (2015).  
 [4] M. Mizumaki, K. Yano, I. Umehara, F. Ishikawa, K. Sato, A. Koizumi, N. Sakai, and T. Muro, *Phys. Rev. B* **67**, 132404 (2003).

- [5] G. B. G. Stenning, G. J. Bowden, S. A. Gregory, J.-M. L. Beaujour, P. A. J. De Groot, G. Van der Laan, L. R. Shelford, P. Bencok, P. Steadman, A. N. Dobrynin, and T. Hesjedal, *Appl. Phys. Lett.* **101**, 072412 (2012).
- [6] K. Dumesnil, S. Fernandez, A. Avisou, C. Dufour, A. Rogalev, F. Wilhelm, and E. Snoeck, *Eur. Phys. J. B* **72**, 159 (2009).
- [7] P. Schattschneider, S. Rubino, C. Hébert, J. Ruzs, J. Kuneš, P. Novák, E. Carlino, M. Fabriziooli, G. Panaccione, and G. Rossi, *Nature (London)* **441**, 486 (2006).
- [8] L. Calmels, F. Houdellier, B. Warot-Fonrose, C. Gatel, M. J. Hÿtch, V. Serin, E. Snoeck, and P. Schattschneider, *Phys. Rev. B* **76**, 060409 (2007).
- [9] Z. Q. Wang, X. Y. Zhong, R. Yu, Z. Y. Cheng, and J. Zhu, *Nat. Commun.* **4**, 1395 (2013).
- [10] D. Pohl, S. Schneider, J. Ruzs, and B. Rellinghaus, *Ultramicroscopy* **150**, 16 (2015).
- [11] P. Schattschneider, M. Stöger-Pollach, S. Rubino, M. Sperl, C. Hurm, J. Zweck, and J. Ruzs, *Phys. Rev. B* **78**, 104413 (2008).
- [12] X. Fu, B. Warot-Fonrose, R. Arras, D. Demaille, M. Eddrief, V. Etgens, and V. Serin, *Appl. Phys. Lett.* **107**, 062402 (2015).
- [13] B. Warot-Fonrose, F. Houdellier, M. J. Hÿtch, L. Calmels, V. Serin, and E. Snoeck, *Ultramicroscopy* **108**, 393 (2008).
- [14] C. Gatel, B. Warot-Fonrose, and P. Schattschneider, *Ultramicroscopy* **109**, 1465 (2009).
- [15] S. Muto, J. Ruzs, K. Tatsumi, R. Adam, S. Arai, V. Kocevski, P. M. Oppeneer, D. E. Bürgler, and C. M. Schneider, *Nat. Commun.* **5**, 1 (2014).
- [16] T. Thersleff, J. Ruzs, S. Rubino, B. Hjörvarsson, Y. Ito, N. J. Zaluzec, and K. Leifer, *Sci. Rep.* **5**, 13012 (2015).
- [17] K. H. J. Buschow, *Rep. Prog. Phys.* **40**, 1179 (1977).
- [18] J. B. Goedkoop, B. T. Thole, G. van der Laan, G. A. Sawatzky, F. M. F. de Groot, and J. C. Fuggle, *Phys. Rev. B* **37**, 2086 (1988).
- [19] B. Sanyal, C. Antoniak, T. Burkert, B. Krumme, A. Warland, F. Stromberg, C. Praetorius, K. Fauth, H. Wende, and O. Eriksson, *Phys. Rev. Lett.* **104**, 156402 (2010).
- [20] A. P. Holm, S. M. Kauzlarich, S. A. Morton, G. D. Waddill, W. E. Pickett, and J. G. Tobin, *J. Am. Chem. Soc.* **124**, 9894 (2002).
- [21] J. Ruzs, O. Eriksson, P. Novák, and P. M. Oppeneer, *Phys. Rev. B* **76**, 060408 (2007).
- [22] E. Dartyge, F. Baudelet, C. Giorgetti, and S. Odin, *J. Alloys Compd.* **275**, 526 (1998).
- [23] P. Carra, B. T. Thole, M. Altarelli, and X. Wang, *Phys. Rev. Lett.* **70**, 694 (1993).
- [24] P. Schattschneider, *Linear and Chiral Dichroism in the Electron Microscope* (Academic, Pan Stanford, 2012), Chap. 8, pp. 129–135.
- [25] See Supplemental Material at <http://link.aps.org/supplemental/10.1103/PhysRevB.94.140416> for details on the useful derivation steps.
- [26] S. Löffler and P. Schattschneider, *Ultramicroscopy* **110**, 831 (2010).
- [27] J. Ruzs, S. Rubino, and P. Schattschneider, *Phys. Rev. B* **75**, 214425 (2007).
- [28] K. Dumesnil, M. Dutheil, C. Dufour, and P. Mangin, *Phys. Rev. B* **62**, 1136 (2000).
- [29] Y. Teramura, A. Tanaka, and T. Jo, *J. Phys. Soc. Jpn.* **65**, 1053 (1996).
- [30] Y. Teramura, A. Tanaka, B. T. Thole, and T. Jo, *J. Phys. Soc. Jpn.* **65**, 3056 (1996).
- [31] C. Piamonteze, P. Miedema, and F. M. F. de Groot, *Phys. Rev. B* **80**, 184410 (2009).
- [32] J. Verbeeck, C. Hébert, S. Rubino, P. Novák, J. Ruzs, F. Houdellier, C. Gatel, and P. Schattschneider, *Ultramicroscopy* **108**, 865 (2008).
- [33] P. Blaha, K. Schwarz, G. K. H. Madsen, D. Kvasnicka, and J. Luitz, *wien2k, An Augmented Plane Wave + Local Orbitals Program for Calculating Crystal Properties* (Karlheinz Schwarz, Technische Universität Wien, Austria, 2001).